Chemical Engineering Journal 549 (2026) 182605

Contents lists available at ScienceDirect

Chemical Engineering Journal

journal homepage: www.elsevier.com/locate/cej

A flexible passive UHF RFID sensor for wireless humidity detection

Jiaqi Zhang [a], Chenbin Zhao [a], Haidong He [b,c], Donglin Wu [a], Enting Gao [d], Changrong Liu [a], Xuemei Lu [e], Tao Peng [f], Baoqing Nie [a,*]

[a] School of Electronic and Information Engineering, Soochow University, Suzhou, Jiangsu, 215006, China
[b] The College of Mechanical and Electrical Engineering, Soochow University, Suzhou, Jiangsu, 215000, China
[c] Jiangsu Provincial Key Laboratory of Embodied Intelligence Robot Technology, Suzhou, Jiangsu, 215000, China
[d] School of Electronic and Information Engineering, Suzhou University of Science and Technology, Suzhou, 215009, Jiangsu, China
[e] Jiangsu Key Laboratory of Biophotonics, Suzhou City University, Suzhou, Jiangsu Province, 215104, China
[f] School of Future Science and Engineering, Soochow University, Suzhou, Jiangsu, 215222, China

ARTICLE INFO

Keywords:
Flexible passive sensor
Wireless humidity sensor
UHF RFID
Dual tag
Respiration detection

ABSTRACT

Flexible wireless humidity sensors hold significant potential in health and environmental monitoring due to simple design, low cost, and wireless capability. Most existing passive wireless humidity sensors rely on an inductor-capacitor (LC) resonant structure. However, their near-field coupling mechanism limits both sensitivity and wireless communication distance. To address these limitations, this paper presents a flexible radio frequency identification (RFID)-based wireless humidity sensor designed for remote humidity detection. The sensor comprises an ultrahigh frequency (UHF) RFID tag deposited with a small piece of MXene/graphene oxide (MGO) composite. The humidity-sensitive MGO layer converts variations in relative humidity into corresponding changes in electrical resistance, which in turn modulates the tag impedance. Consequently, the tag impedance variations induce the received signal strength indication (RSSI) changes, which is wirelessly detected by a RFID reader. Importantly, the MGO composition and deposition location are selected across distinct antenna regions to align the humidity-induced resistance variation with the most impedance-sensitive regime. The sensor has a high sensitivity (0.45 dBm/% RH) with a low hysteresis (of 2.9% RH) over a relative humidity range of 19–96% RH. Additionally, a dual-tag sensing structure is introduced to effectively mitigate distance-dependent signal variations between the sensing tag and the reader, thereby significantly enhancing measurement reliability in practical scenarios. This dual-tag architecture provides a validated architecture-based solution to the distance-sensitivity challenge that previous passive wireless sensors have largely avoided. The maximum wireless transmission distance of the dual-tag structure is more than 30 cm. To demonstrate the potential utilization, the UHF RFID humidity sensor successfully measures the frequency of respiration in a wireless manner. The UHF RFID-based humidity sensing technology holds promise for assessing respiratory abnormalities.

1. Introduction

Humidity is one of the most significant variables encountered in daily life [1–3], and its applications permeate diverse aspects including industrial manufacture, agricultural production, intelligent home and health monitoring [4–6]. The detection of humidity relies on humidity sensors, thus making humidity sensors play a crucial role in these active areas [7,8]. For example, flexible humidity sensors enable continuous respiratory monitoring in a real-time manner [9–11], and can provide essential physiological indicators such as respiratory rate and depth in medical care for breath detection. However, long-term continuous monitoring of these signals (e.g., respiratory) using hard-wired sensors worn on the body poses risks of restricting body movements or causing wire connection failures [12,13]. Thus, it is required that humidity sensors can be comfortably worn without complicated wire connection for long-term physiological signal detection scenarios [14].

Flexible passive wireless sensors have gained tremendous popularity owing to their independence from onboard batteries, wireless connectivity, and ability to perform without active devices [15,16]. For passive wireless humidity sensors, the majority of existing studies rely on an LC resonant structure [17,18]. Humidity-sensitive materials, such as metal oxides, graphene oxide (GO), and their composites, are usually coated

* Corresponding author.
E-mail address: qixinbq@suda.edu.cn (B. Nie).

https://doi.org/10.1016/j.cej.2026.182605
Received 22 June 2026; Received in revised form 12 August 2026; Accepted 29 September 2026
Available online 1 October 2026
1385-8947/© 2026 Elsevier B.V. All rights are reserved, including those for text and data mining, AI training, and similar technologies.

onto the surface of the LC resonator. As humidity changes, these materials alter the equivalent capacitance of the LC structure, thereby shifting its resonant frequency. Lv et al. proposed an LC passive wireless humidity sensor utilizing a composite of multi-walled carbon nanotubes and tungsten disulfide as the sensing material [19]. The sensor operates within a humidity range of 15% RH to 95% RH, exhibiting a sensitivity of 70.6 kHz/%RH in the 15%RH to 55% RH range. Meanwhile, Miao et al. developed a sensor based on molybdenum disulfide as the sensing material, integrated with a neural network algorithm to achieve simultaneous temperature and humidity detection [20]. This sensor achieved a sensitivity of 107.2 kHz/%RH across a humidity range of 70% RH to 95% RH. Despite their advantages such as a compact size, low cost, and low power consumption, passive LC humidity sensors suffer from low device sensitivity and a short wireless communication distance due to the near-field electromagnetic coupling mechanism.

On the other hand, ultra-high-frequency (UHF) radio frequency identification (RFID) sensing technology serves as an important passive wireless sensing solution [21]. The UHF passive RFID sensing technique actives in the frequency range of 860 to 960 MHz, and is able to operate in a longer communication distance which is typically tens of meters [22]. A typical UHF RFID sensing system consists of a RFID tag integrated with a sensing element. Variations in external stimuli (e.g., humidity) alter the electrical properties (e.g., resistance, capacitance, or inductance) of the sensing component, thereby modulating the operational state of the tag. When the tag is illuminated by electromagnetic waves from a reader, the backscattered signal at the tag's resonant frequency shifts in accordance with these stimuli [23,24]. As a result, this approach enables humidity detection by monitoring the wireless backscattered signal strength (RSSI). To the best of our knowledge, there have been few reports on UHF RFID-based wireless humidity sensors. A similar configuration has been utilized for wireless ammonia detection [25]. Owing to the use of the UHF band, this scheme not only maintains high sensitivity but also achieves a significantly longer wireless communication distance (up to half a meter) compared to LC resonator-based systems.

In this report, we present a passive wireless sensor based on UHF RFID technology for remote humidity monitoring. The sensor is constructed in a simple architecture, including a thin RFID tag (a 3D omnidirectional planar dipole array antenna and an IC chip) and a piece of humidity-sensitive sensing material depositing on a part of the tag (Fig. 1a). The whole sensor is a thin film-like structure with high flexibility and a compacted dimension (50 mm × 50 mm × 0.06 mm), which is the thinnest UHF RFID wireless humidity sensor to our best knowledge. Specifically, the moisture sensitive material named MGO consists of single layer $Ti_3C_2T_x$ MXene and graphene oxide (GO), which is highly sensitive to the ambient humidity. When the surrounding humidity environment changes, water molecules will combine with the functional groups on the MGO surface through absorption. As a result, the resistance of the MGO increases, and in turn the equivalent impedance of the tag antenna changes accordingly. Therefore, impedance mismatch between the antenna and the chip reduces the received signal strength indication (RSSI) measured by an external RFID reader, which forms the basis for humidity sensing. Importantly, this work systematically bridges the material's electrical properties with the antenna's impedance response and spatial sensitivity distribution. The key design parameters have been optimized, which include the component mass ratio of MXene and GO, and the relative position of the sensing material to the tag. The UHF RFID wireless humidity sensor achieves a high sensitivity (0.45 dBm/%RH) over a relative humidity range of 19–96% RH. The sensor exhibits a low hysteresis (the hysteresis error is within 2.9% RH) and excellent repeatability. Furthermore, since the RSSI is intrinsically sensitive to the communication distance between the sensor and the reader, a dual-tag sensing structure has been utilized for a robust humidity detection in application demonstration. The UHF RFID humidity sensor has successfully measured the respiratory frequency in different wireless communication distances. The results reveal the great prospect of the sensor in the area such wearable electronics and smart physiological signal monitoring devices.

2. Material and methods

2.1. Device fabrication process

The UHF RFID tag used in this work is a commercially available product (model: BYH-KH47, manufacturer: Shenzhen Bo Yu Heng Technology Co., LTD). It incorporates a NXP SL3S1206 UCODE 9 IC with an impedance of 10 – j191 Ω at 915 MHz. The antenna is a 3D omnidirectional planar dipole array printed on a flexible PET substrate with a thickness of 0.06 mm. The fabrication process of the flexible passive humidity sensor is shown in Fig. S1 in *Supplement Material*. The fabrication process started with preparation of MXene and GO solution (MGO solution). The moisture-sensitive conductive composites were

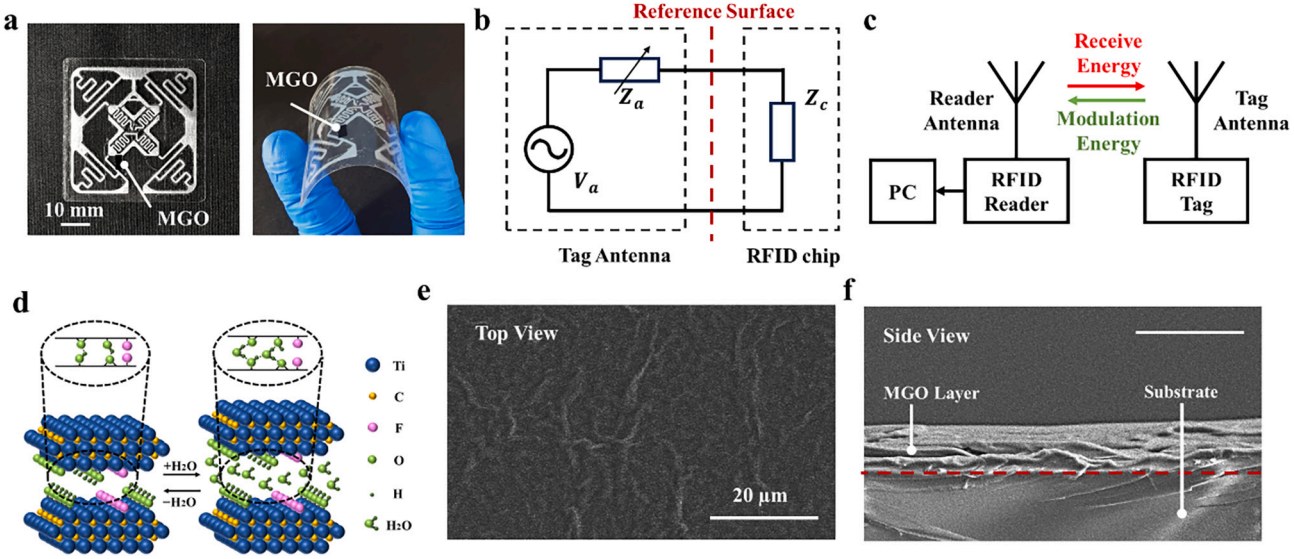

Fig. 1. (a) Photograph of the UHF RFID humidity sensor. (b) Equivalent circuit diagram of the humidity sensor. (c) Block diagram of the RFID wireless transmission system. (d) Schematic illustration of hydration and dehydration process of the MXene. (e) Top view of the SEM image of the MGO. (f) Side view of the SEM image of the MGO. Scale bar: 20 μm.

synthesized by mixing MXene solution (5 mg/ml, $Ti_3C_2T_x$, FoShan XinXi Technology Co., Ltd) with GO solution (2 mg/ml, Shenzhen Suiheng Technology Co., Ltd) in a centrifuge tube at a mass ratio of 1:0, 5:1, or 20:1, and then dispersed by ultrasonic dispersion for 30 min using an ultrasonic processor to ensure that the two solutions were well mixed. Next, a vortex mixer was used for 10 min to obtain a homogeneous mixed MGO solution.

In the second step, an acrylic plate layer (90 μm thickness) was laser-machined to create a mask containing a 5 mm × 2.5 mm rectangular opening. The RFID tag surface was rigorously cleaned using ethylene diacetate and ethanol, then subjected to vacuum oxygen plasma treatment for 20 s to enhance surface wettability. Aligning with the predefined markers, the mask was placed over the feed point of the tag antenna. Using a micropipette, 2.0 μl of the synthesized MGO solution was deposited into the masked area. The sample was subsequently placed in a drying oven at 25 °C for 3 h to facilitate complete solvent evaporation. Finally, the mask plate was removed and an UHF RFID humidity wireless sensor was obtained.

2.2. Sensor performance characterization

In order to investigate the sensing performance of the wireless humidity sensor, saturated salt solutions were used as the standard humidity source. The principle is based on the three-phase equilibrium system of salt and water vapor: after dissolving analytically pure salt (e.g., LiBr, NaCl, etc.) in pure water, the salt molecules ionize and form a hydrate with the water molecules. At the same time, a dynamic equilibrium is established between the liquid surface and the gas-phase space (with the water molecules evaporating at the same rate as the condensation rate), and a stable relative humidity field is eventually formed at the top of the airtight container. To construct a gradient humidity environment, seven salts were selected to prepare saturated solutions, which are lithium bromide (LiBr), magnesium chloride ($MgCl_2$), potassium carbonate (K_2CO_3), sodium bromide (NaBr), sodium chloride (NaCl), potassium chloride (KCl) and sodium dihydrogen phosphate (NaH_2PO_4).

The humidity characterization system is shown in Fig. S2 in *Supplement Material*, including the wireless humidity sensor, a RFID reader (R200-C70, Shenzhen IOT Technology), a computer and seven sets of saturated salt solutions (19% RH, 37% RH, 43% RH, 54% RH, 68% RH, 78% RH, 96% RH). The sensor tags were placed in a closed container with different humidity salt solutions, and RSSI was collected in real time by the RFID reader and transmitted to the host computer. The system operated at a constant temperature of 22 °C ± 2 °C (Fig. S3), and the distance between the reader antenna and the tag was fixed at 10 cm to exclude environmental interference and ensure RF signal stability. This study was approved by the Medical Ethics Committee of Soochow University (2024CS124), Suzhou, China. All the participants consented to participate in the study and signed the written informed consent.

3. Results and discussion

3.1. Operating principle

The humidity signal transmission relies on the classical UHF RFID (915 MHz) wireless communication technique. As aforementioned, the RFID tag consists a tag antenna, a RFID chip and a small moisture-sensitive MGO block which covers on the antenna surface. Fig. 1b illustrates the equivalent circuit diagram which includes of an impedance of the dipole-type antenna ($Z_a = R_a + jX_a$), and an impedance of the RFID chip ($Z_c = R_c + jX_c$). V_a represents the open circuit voltage at the dipole antenna. In Fig. 1c, when the electromagnetic wave generated by the RFID reader impinges on the RFID tag antenna, the tag antenna harvests energy from the RF signal and actives the corresponding RFID chip and back-scatters the relevant information in the chip to the RFID reader. After the reader antenna receives the signals, the reader can decode the information and determine the RSSI value. The value of RSSI can be expressed in a simplified as (see detail derivation in *Supplement Material*):

$$RSSI = G_r + K \tag{1}$$

where K represents the received signal strength from the reader excluding the gain of the sensor tag G_r. The K is related to several factors, such as the transmitting power of the reader, the gain of the reader antenna, the path loss in the transmission of electromagnetic waves. It can be estimated as a constant as long as the structure of the reader antenna and the separation distance between the reader and the sensor remain unchanged.

The G_r in Eq. (1) indicates actual gain of the tag antenna, which can be expressed by the following Eq. [26]:

$$G_r = \frac{4R_cR_a}{|Z_c + Z_a|^2} \times G_{max} \tag{2}$$

The maximum value of the G_r is achieved when the Z_c is conjugate to the Z_a, indicating the optimal match between the antenna and the chip. According to Eqs. (1) and (2), the RSSI decreases as the impedance of the antenna Z_a and the chip Z_c losses the optimal match.

3.2. Working principle of the UHF RFID humidity sensor

As the humidity sensitivity material, it has to absorb/desorb water molecular in a fast rate, and its resistance change in the entire humidity range should allow a large RSSI variation. Here, the single layer $Ti_3C_2T_x$ MXene and graphene oxide mixture are chosen as the humidity sensing material. As shown in Fig. 1d, the surface of MXene is rich in functional groups (e.g., -OH, —O, and —F, etc.). When the MXene is exposed to a moisture environment, water molecules likely bind to the functional groups through absorption, resulting in a change in the electrical conductivity of MXene [9,27]. GO retains a large number of oxygen-containing functional groups, such as carboxyl group (-COOH) and epoxy group (-C-O-C) [28]. The hydrogen bonds make GO and MXene layers attractive to form hybrid assemblies [29]. As shown in Fig. 1e and f, the sensing material has a layered structure. When the material absorbs water molecules, the gaps between electrical path increase, thereby increasing the resistance. The addition of GO leads to the enhancement of hydrogen bonding with water molecules, which further enhances the change of electrical conductivity of the material. However, excessive GO will generate a large resistance, making the variation of the RSSI too low to be detected. Therefore, an appropriate mixture ratio of MXene and GO should be investigated [30,31].

As aforementioned, the moisture-sensitive material MGO in the sensor replaces part of the electrode region of the tag antenna, which results in a mismatch between the antenna impedance Z_a and the chip impedance Z_c. When the external humidity environment changes, it causes the variation of the MGO resistance, which varies the degree of the impedance mismatch between Z_a and Z_c. According to Eqs. (1) and (2), the RSSI changes accordingly. In order to improve the responsiveness of the sensor to humidity, this paper optimizes the covering location of the MGO on the antenna and the resistance variation range of the MGO in both simulation analysis and experimental investigation.

3.3. Sensor antenna simulation analysis

To achieve a high RSSI response to humidity variation, the resistance change of the MGO should be optimized in the entire humidity range to produce a largest RSSI variation. Finite element method has been used to determine the optimal resistance fluctuation range. The antenna gain, return loss, impedance and electric field distribution of the original tag antenna have shown in Fig. S4 in *Supplement Material*. The maximum gain is 0.09 dB and the return loss *S11* is less than −30 dB at 915 MHz. The impedance of the antenna is well match to that of the chip. By filling

resistance in a slot on the aluminum trace of the antenna (Fig. 2a), the gain and return loss dramatically change. Fig. 2b shows the return loss *S11* changes as the filling resistance in the slot increase from 0 to 3 kΩ. The *S11* of the antenna show a large decrement from −26.08 dB to −32.16 dB as the resistance rises from 0 to 1000 Ω. As the resistance exceeds 1800 Ω, the *S11* keeps almost a constant of −34.4 dB. To calibrate the humidity - antenna impedance, we performed numerical simulations using ANSYS HFSS to analyze the antenna impedance as a function of the MGO layer's resistance variation at 915 MHz (Fig. 2c). As the R_{MGO} increases, both the real and imaginary parts of the antenna impedance increase. Fig. 2d provides the 3D gain of the antenna with different filling resistance values of 50 Ω, 500 Ω, and infinity. Obviously, as the filling resistance becomes smaller, the gain of the antenna turns into small and losses its spatial symmetry.

3.4. Effect of the deposition position on the sensing performance

According to the simulation results, the location where the MGO deposited on the antenna is an important factor to the device sensitivity. Here, five representative deposition positions are strategically selected across distinct physical regions of the tag antenna (Fig. 3a): the capacitive regions dominated by metallic gaps (P2 and P3), the inductive regions along the serpentine meandering lines (P4 and P5), and the junction connecting the ohmic-loss resistance and radiation-resistance regions (P1). A standard resistor (resistance range 0–3 kΩ, tolerance 1%, 0603 package) is soldered on each location, and the corresponding RSSI is recorded by the reader. As shown in Fig. 3b, the RSSI value exhibits a similar trend under the P2-P5 scenarios: all the RSSI values show a rapid decrease with increasement of resistance values, after which the RSSI values keep almost the same at high resistance values. Differently, the RSSI exhibits an opposite trend with the changes of the resistance values in the P1 region. The maximum RSSI variation is around 20 dBm in the 0–510 Ω interval. The changes of the RSSI along with the resistances in other four regions are all smaller than that in P1 probably because the P1 region is situated at the location where the antenna exhibits the strongest incident coupling and its equivalent impedance is most sensitive to resistance variations. Obviously, the sensing performance of the P1 region is significantly better than the other regions and therefore P1 is finally identified as the optimal deposition location for the humidity-sensitive material.

3.5. Effect of the MXene/GO mass ratios on the sensing performance

According to the simulation and experiment results, achieving a high humidity response requires that the MGO resistance variation remains within 510 Ω across the full humidity range. Here, the humidity-resistance response of the moisture-sensitive material with different MXene and GO mass ratios has been investigated. Fig. 3c shows the experimental calibration of the MGO resistance response to varying relative humidity levels. A 2 mm × 2 mm MGO sample was placed in a humidity-controlled chamber and connected to an impedance analyzer via electrical wires for resistance measurement. Fig. 3b illustrates the resistance changes of the MGO along with the humidity ranging from 19% RH to 96% RH under different MXene to GO mass ratios of 1:0, 20:1, 5:1. Three samples in each ratio have been used for characterization. As aforementioned, the MXene-GO composite possesses a layered structure containing numerous hydrophilic groups. Upon water absorption, these groups facilitate the expansion of interlayer gaps and an increase in electrical pathways. Specifically, GO contains abundant oxygen-containing functional groups. The introduction of GO enhances the overall water absorption capability of the composite, thereby broadening the range of resistance variation.

As shown in Fig. 3d-3e, the resistance value of the pure MXene (without GO) is 16.8 Ω under humidity level of 19% RH, and its resistance change ΔR in the entire humidity range from 19% RH to 96% RH is 13.3 Ω. In comparison, the resistance change ΔR increases to 27.7 Ω in the whole humidity range under the MXene/GO mass ratios of 20:1, which is 2-fold higher than that of the pure MXene. At the 5:1 ratio, the

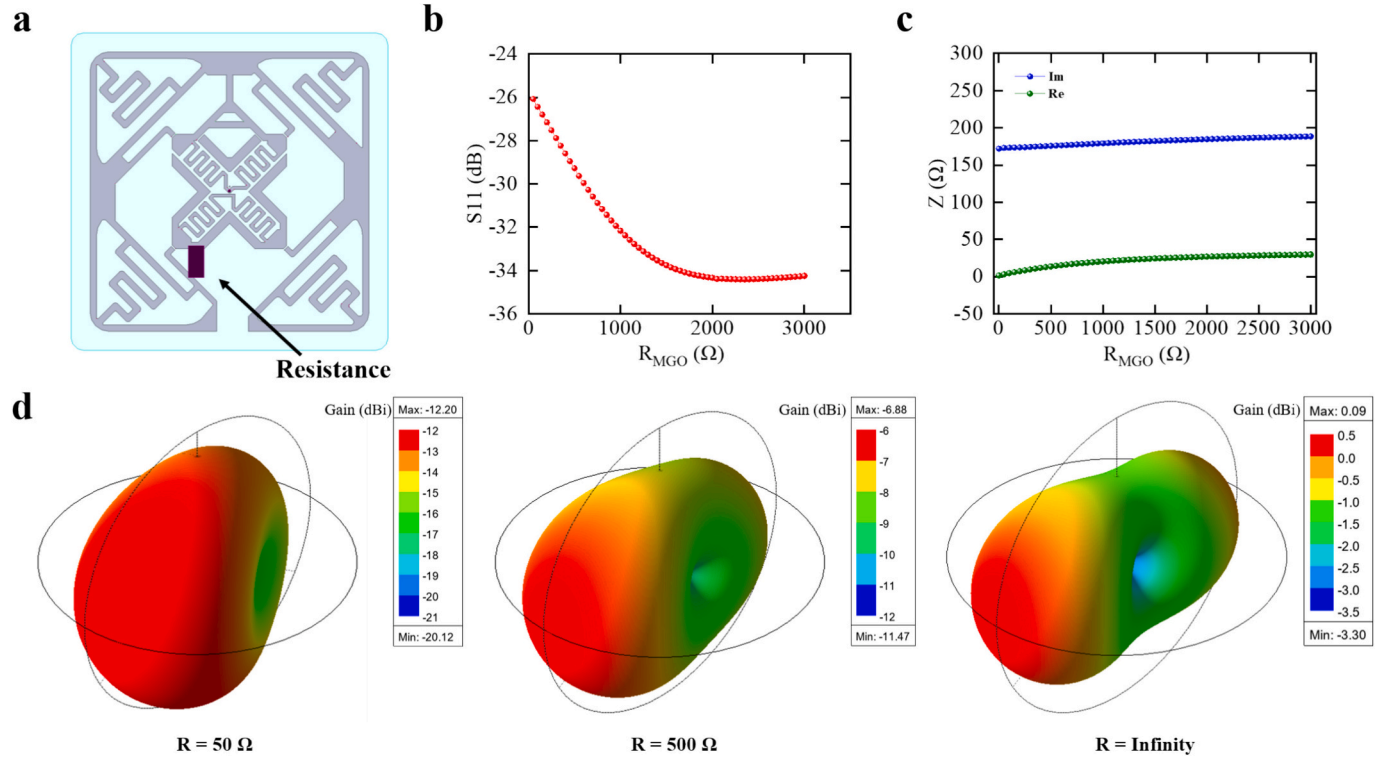

Fig. 2. (a) Simulation model of the sensor antenna filling with different values of resistances. (b) The relationship between the return loss *S11* of the tag antenna and the resistance value of MGO. (c) The relationship between the impedance of the tag antenna and the resistance value of MGO. (d) Simulation results of the 3D gain of the tag antenna, where the resistance values are 50 Ω, 500 Ω, and infinity, respectively.

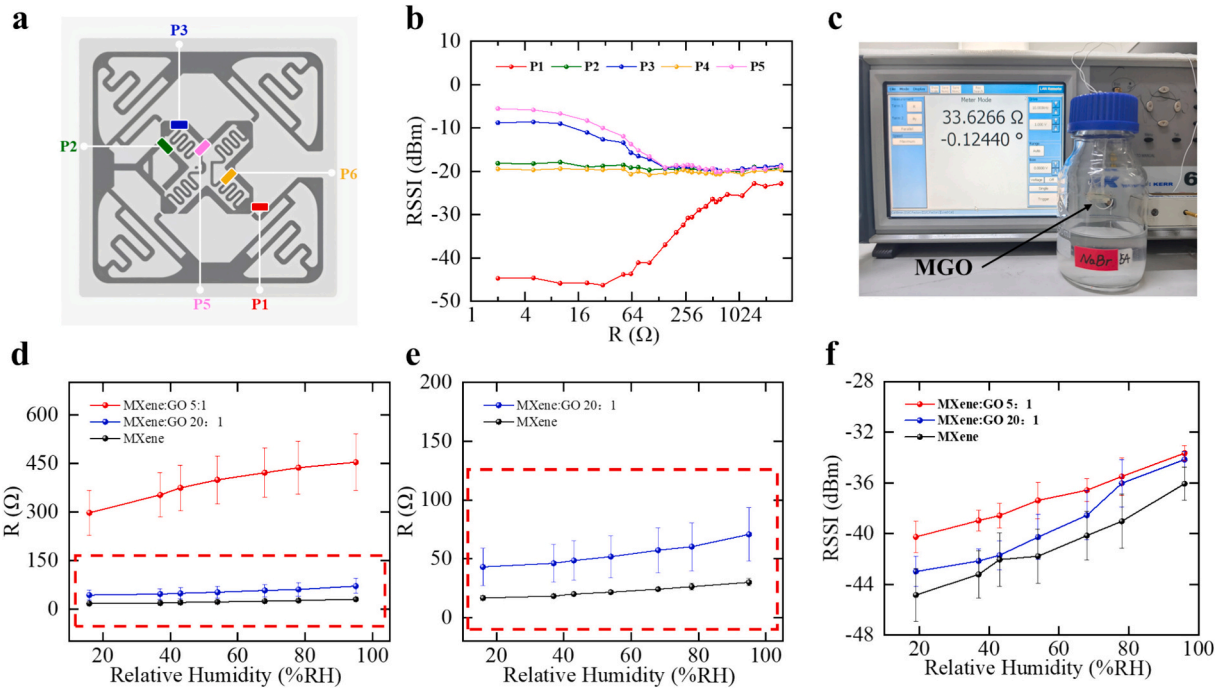

Fig. 3. (a) Illustration of five different locations of the tag antenna noted as P1 - P5 where the MGO is separately deposited on. (b) RSSI changes when different resistors are connected to the antenna at the locations of P1 - P5. (c) Photograph of the experimental setup for MGO resistance measurement under different humidity conditions. (d-e) Resistance changes of the MGO with different MXene/GO mass ratios at relative humidity ranging from 19% to 96%. (f) Relationship between ΔRSSI and relative humidity when the MGO is deposited on P1 under different MXene/GO mass ratios.

resistance spans 300 Ω to 460 Ω across the full humidity range. This phenomenon accords with the hypothesis as aforementioned, which the addition of GO into MXene facilities to increase the water absorption ability. Further GO loading would raise both the baseline and the humidity-induced resistance variation, but the maximum resistance would exceed 510 Ω, which is the upper bound of the antenna's most sensitive impedance window (Fig. 3b).

The device sensitivity of the wireless humidity sensor has been characterized experimentally. According to the finding in the previous sections, P1 region is optimal location for the MGO deposition. Here, the humidity sensors with different MXene/GO ratios were placed in the closed container with a saturated salt solution for 600 s, and the RSSI value was measured by the RFID reader wirelessly. Fig. 3f shows the relative RSSI changes of the sensors with MXene/GO mass ratios of 5:1, 20:1, 1:0 in the entire humidity ranges. The sensitivity of the sensor with a 5:1 MGO ratio is 0.086 dBm/%RH, while the sensitivities of the pure MXene and 20:1 MGO devices are both 0.11 dBm/%RH. These results are inconsistent with those measured from the resistance test (Fig. 3d). It is speculated that the contact resistance between MGO and the electrode differs between the two conduction paths due to the use of different electrode materials (aluminum for the tag and silver tape for the resistance test). Meanwhile, the effective area of the MGO sample on the tag is approximately twice that of the sample used in the resistance test, resulting in increased resistance and sensitivity. Considering that pure MXene is prone to oxidation, leading to unstable data (larger standard deviation), all subsequent experiments are conducted using the sensor with a 20:1 MGO ratio.

3.6. Characterization on the MXene/GO with different mixing ratios

To further investigate the material properties of the MXene/GO composites with different mixing ratios, we have characterized the three formulations using Raman spectroscopy, Fourier-transform infrared spectroscopy (FTIR), X-ray diffraction (XRD), and X-ray photoelectron spectroscopy (XPS). For simplicity in material characterization, the composites with mixing ratios of 5:1 and 20:1 are hereafter denoted as MGO5 and MGO20, respectively. XPS analysis reveals the elemental composition and chemical bonding evolution of the composite films. As shown in Figs. 4a–4c, the survey spectra of all three samples exhibit characteristic peaks of Ti, C, O, and F. The high-resolution C 1 s spectra show that the C—Ti peak intensity progressively decreases with increasing GO content. Similarly, in the O 1 s spectra, MGO5 displays the highest relative intensity of the C—O signal. From pure MXene to MGO20 and MGO5, the relative abundance of oxygen-containing functional groups increases, confirming the successful incorporation of GO into the composite. Fig. 4d presents the Raman spectra of the three formulations. The Raman peaks at 197, 281, and 382 cm^{-1} are attributed to the A_1g vibrational mode of Ti and the Eg molecular vibrations involving both Ti and C atoms in the in-plane modes. In the MGO5 spectrum, two additional peaks at 1345 and 1599 cm^{-1} are clearly observed, corresponding to the D band and G band of GO, respectively [31]. FTIR spectra are shown in Fig. 4e. Pure MXene exhibits absorption bands associated with O—H, C═C, and Ti—O vibrations. MGO5 and MGO20 show enhanced C–O/C–O–C features in the 1000–1300 cm^{-1} region. The peaks in the grey-shaded region are attributed to the PET substrate [32]. XRD patterns of the composites are presented in Fig. 4f. The $Ti_3C_2T_x$ MXene pattern displays a sharp peak at $2\theta = 6.58°$, while MGO20 and MGO5 exhibit peaks at $2\theta = 7.06°$ and 7.68°, respectively. The shift toward higher diffraction angles reflects a decrease in the interlayer spacing [31].

3.7. Dynamic responses of the wireless humidity sensor

The wireless humidity sensor's RSSI responses to increasing and decreasing humidity are shown in Fig. 5a. During the humidification process, the RSSI increases monotonically with rising relative humidity. During the dehumidification process, the descending curve closely overlaps with the ascending one, indicating that the sensor response exhibits good reversibility with respect to humidity variation. The maximum offset between the humidification and dehumidification

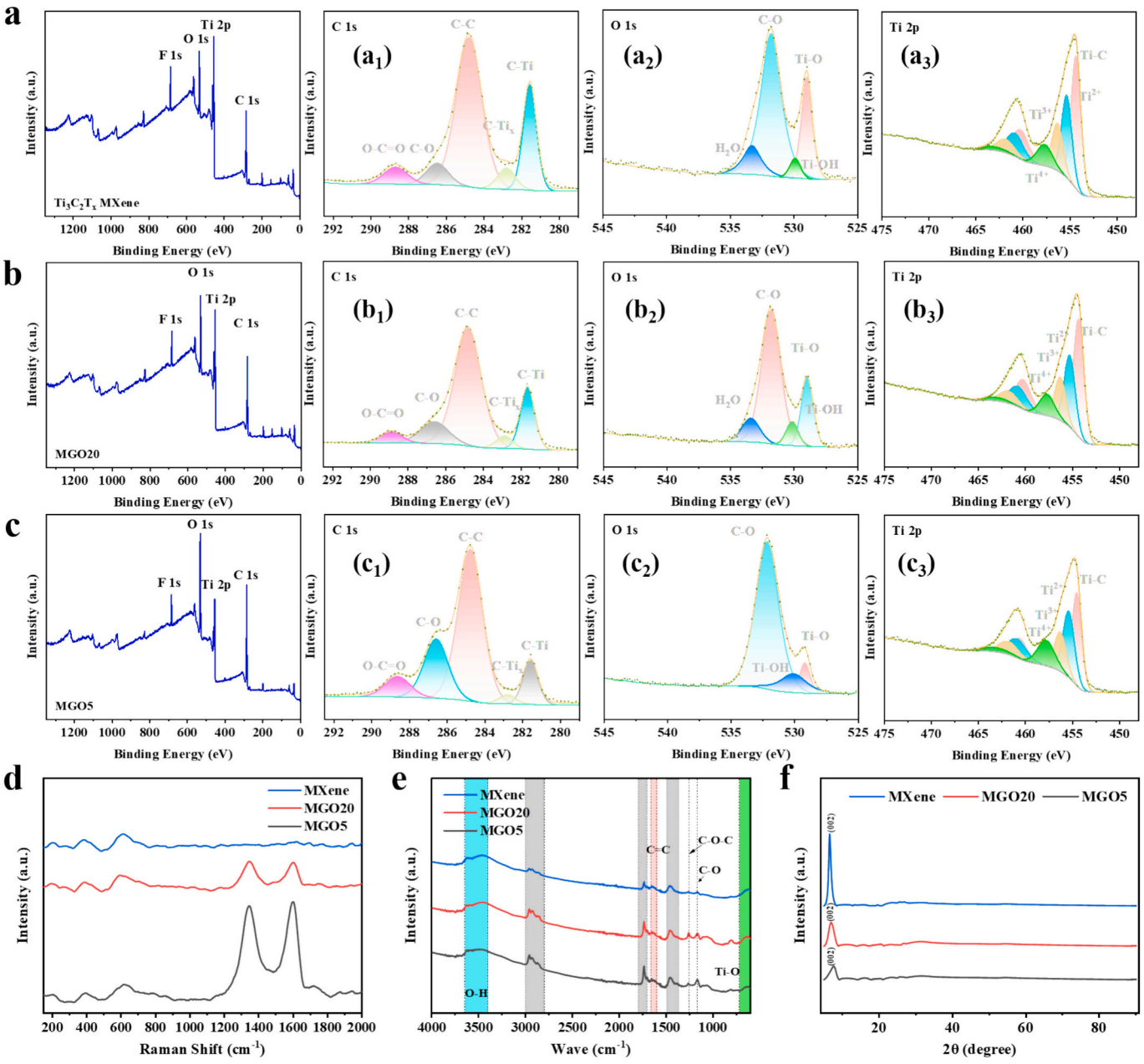

Fig. 4. Material characterizations of MXene, MGO20 and MGO5: (a–c) XPS survey spectra and the corresponding high-resolution (a_1–c_1) C 1 s, (a_2–c_2) O 1 s, and (a_3–c_3) Ti 2p peak-fitting spectra. (d) Raman spectra, (e) FTIR spectra and (f) XRD patterns of MXene, MGO20 and MGO5.

curves is approximately 2.9% RH. Fig. 5b presents the sensor's RSSI response under cyclic humidity steps between 60% RH and 96% RH. The stable and repeatable RSSI fluctuations confirm the sensor's reliable repeatability under dynamic humidity changes. In addition, by analyzing the rising and falling edges in Fig. 5b, the response and recovery times can be obtained. As shown in Fig. 5c, the response time (T_{res}) of the sensor upon transitioning from the low-humidity state to the high-humidity state is approximately 8.2 s, while the recovery time (T_{rec}) from high humidity back to low humidity is about 11.4 s. Fig. 5d compares the RSSI–humidity curves of the wireless humidity sensor measured on day 1, day 3, and day 5. The maximum deviation among the three curves is 6.5%, indicating that the wireless humidity sensor exhibits good long-term stability over the tested period.

3.8. Effect of dual-tag humidity sensing architecture on device performance

According to Eq. (1), the RSSI value of the sensor tag is not only influenced by the humidity (directly changes the G_r), but also influenced by environmental factors (relevant to the K), such as the communication distance of the sensor and the reader. The sensor-reader distance inevitably changes in actual applications. In order to reduce the potential interferences from the tag-reader distance, we have constructed a dual-tag humidity sensing structure which includes two tags: one is the sensing tag, and the other is a reference tag that is a same type RFID tag without disposing the MGO (Fig. 6a). Fig. 6b-c is the RSSI variations of the sensing tag and the reference tag in response to the relative humidity change at different tag-reader distances. It can be seen that the $RSSI_1$ of the sensing tag is not only sensitive to the humidity but also influenced by the distance. As the humidity keeps unchanged in 90% RH, the RSSI

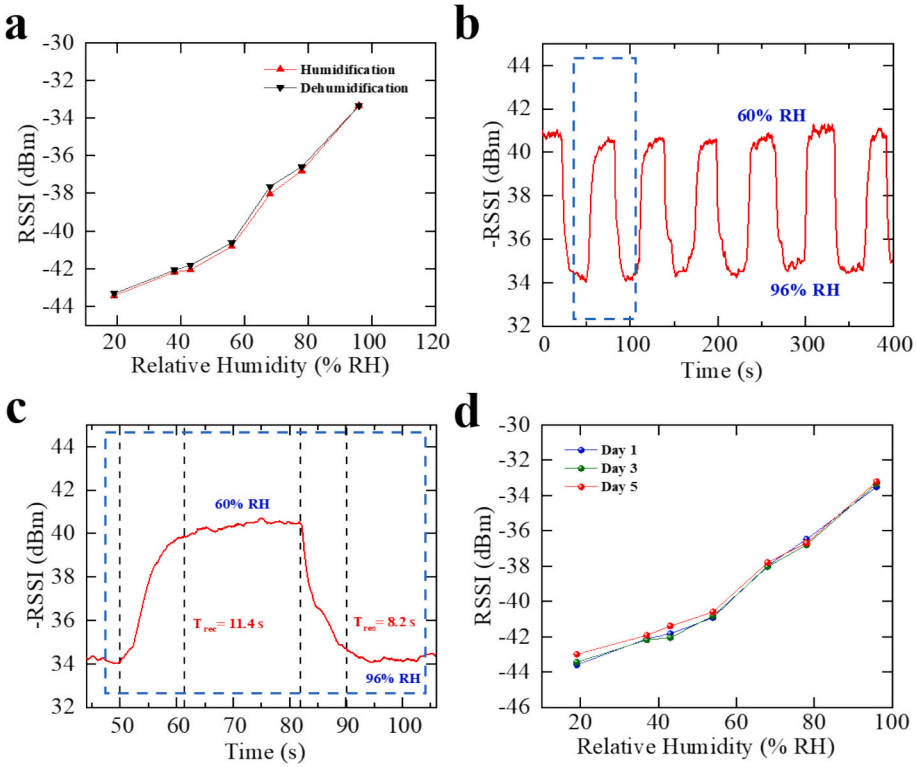

Fig. 5. (a) RSSI-humidity relationship during humidification and dehumidification processes. (b) Repeatability tests of the MGO sensor under the humidity of 60% RH and 96% RH. (c) Characterization on the response/recovery time of the wireless humidity sensor. (d) Long-term stability test of the sensor.

value increases by 11.9 dBm as the communication distance rises from 10 cm to 30 cm. In comparison, the $RSSI_2$ of the reference tag is only sensitive to the communication distance in low humidity level. After the relative humidity is larger than 63% RH, the $RSSI_2$ slightly decrease along the increment of the RH values. This is probably because the optimized impedance matching of the sensing tag induces a load-pull effect in the near field, causing a redistribution of electromagnetic energy that reduces the available incident field strength for the reference tag, thereby lowering its RSSI value [33]. To minimize the distance impact on the RSSI value, the difference between $RSSI_1$ and $RSSI_2$ ($RSSI_1$ - $RSSI_2$) has been utilized to characterize the sensitivity. As shown in Fig. 6d, the device sensitivity (defined as ($RSSI_1$ - $RSSI_2$)/RH) is independent with the communication distances. The sensitivities (from 56% RH to 90% RH) under different distances of 10 cm to 30 cm are about 0.452 dBm/%RH, which indicates the effect of communication distance variation is largely reduced.

To investigate the potential influence of electromagnetic mutual coupling or energy competition between the two tags on the differential RSSI output, a series of experiments have been designed to examine the effects of tag spacing, relative orientation, and multipath propagation. Under ambient conditions of 58% RH and a fixed reader–tag distance of 12 cm, the center-to-center spacing between the two tags is varied from 5 to 15 cm (Fig. 6e, left panel). The fluctuation of the differential RSSI is observed to be 17.08%, which is significantly lower than that of a single-tag RSSI (37.5%). This indicates that the differential architecture effectively suppresses the interference caused by mutual coupling. Furthermore, when the plane of the reader coil is rotated (Fig. 6e, right panel), the differential RSSI output exhibited fluctuations of less than 4.6% over a full 360° rotation. This advantage is attributed to the omnidirectional radiation characteristic of the tag antenna design. However, under other configurations—such as rotation of the reference tag or rotation of the reader coil around the tag array (Fig. S5a-d)—more pronounced variations have been observed. In addition, the sensor maintains stable differential RSSI outputs across different testing environments, confirming that the influence of multipath effects is negligible (Fig. S5e-f).

3.9. *Respiratory monitoring based on the UHF RFID wireless humidity sensor*

Human respiration parameters such as respiratory frequency serve as important indicators of clinical health assessment [34]. Fig. 7a illustrates a conceptual scenario of the proposed UHF wireless humidity sensor for respiratory detection during sleep. Fig. 7b shows the experimental setup for real-time respiration detection. The dual-tag wireless humidity sensor is stuck inside of a mask. A male volunteer aged 24 wears the mask and lies down to mimic the sleep state. The reader is placed on the top of the volunteer's head with a distance about 10 cm (Fig. 7c). The volunteer performs fast breathing, normal breathing, deep breathing, and breath-holding. The real-time RSSI signals of the two tags have been recorded by the reader simultaneously.

Fig. 7d illustrates the time-resolved $RSSI_1$ - $RSSI_2$ of the dural tag sensing system. A zoomed-view images during normal and fast breathing are shown in Fig. 7e and f, respectively. The dual-tag humidity sensing mask is able to effectively distinguish among different respiratory states by the cyclic peaks on the time-resolved $RSSI_1$ - $RSSI_2$ curves. Significant differences of $RSSI_1$ - $RSSI_2$ amplitude and frequency are recognized during normal, deep and rapid breathing. For the normal breathing, the respiratory rate of the volunteer is about 12 breaths/min. The breath rate decreases to 6 breaths/min for deep breaths. The volunteer breathes rapidly up to 20 breaths/min in fast breath state. When the volunteer holds his breath to mimic the apnea, the periodic variation of $RSSI_1$ - $RSSI_2$ disappears, and the values gradually decreases from 30.2 dBm to 22.2 dBm. The signal drift is possibly attributed to the fact that the humidity level inside the mask decreases continuously when the breath is held. Importantly, the output of the wireless humidity sensor is not affected by the reader-tag distance due to the dual-tag architecture. Fig. 7g shows the $RSSI_1$-$RSSI_2$ values of the dual-tag

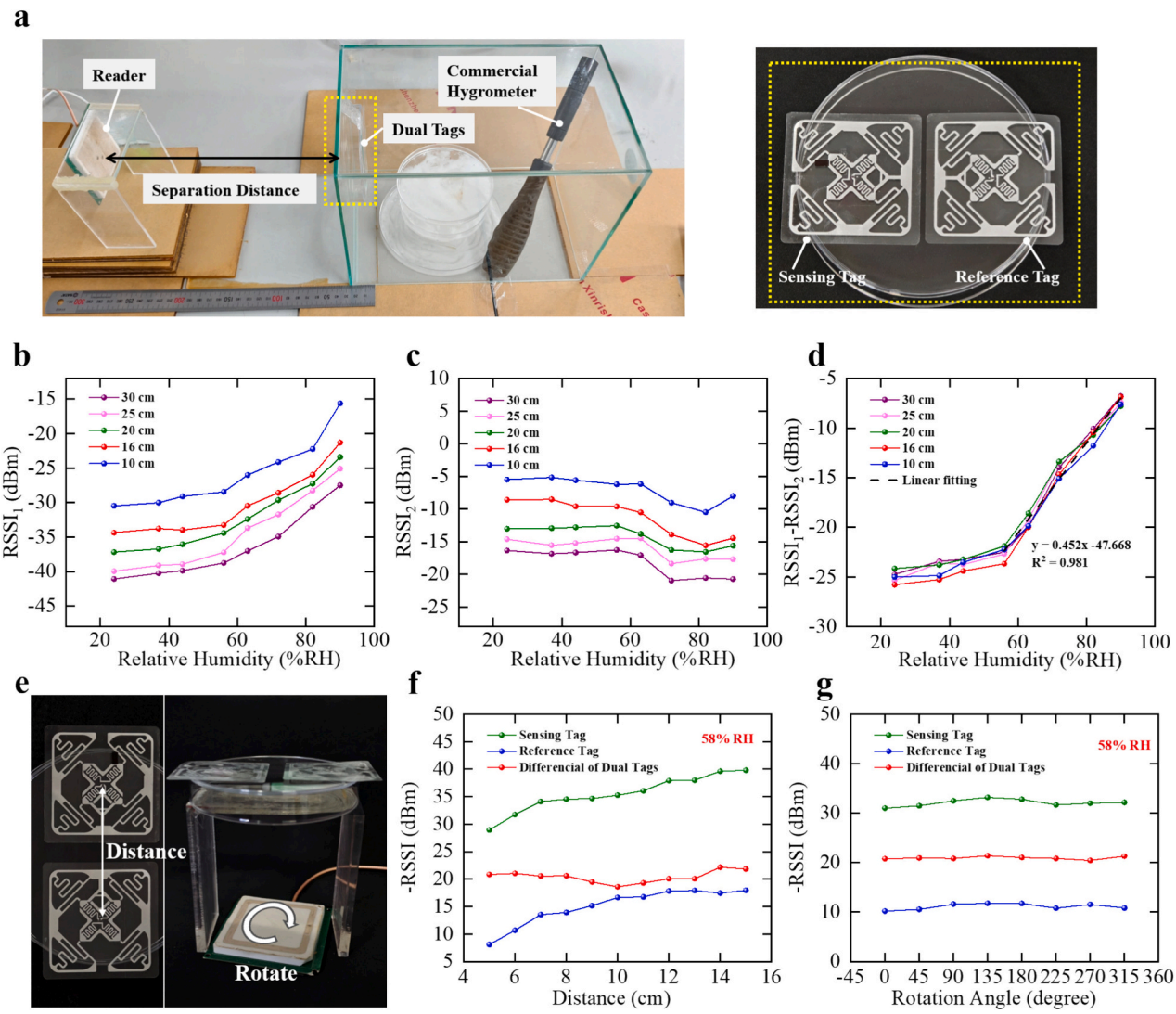

Fig. 6. (a) Image of the experimental setup to characterize the communication distance influences on the dural-tag structure. (b) Relationship between the $RSSI_1$ and relative humidity under different separation distances between the sensing tag and the reader. (c) Relationship between and relative humidity at different separation distances between the reference tag and the reader. (d) Relationship between the $RSSI_1$ - $RSSI_2$ and relative humidity under different separation distances between the two tags and the reader. (e) Photographs of the experimental setup for evaluating the effects of tag spacing and reader coil position on the RSSI. (f) RSSI values of the sensing tag, the reference tag, and their differential signal as a function of the distance between the two tags. (g) RSSI values of the sensing tag, the reference tag, and their differential signal as a function of the relative orientation between the reader coil and the dual tags.

wireless humidity sensor under a normal breathing condition at different communication distances. The amplitude of the $RSSI_1$-$RSSI_2$ keeps around 6.8 dBm with 1.5% variations when the distance increases from 10 cm to 25 cm, indicating the dual-tag topology effectively decreases the effect from the tag-reader distances.

To further validate the reliability of the proposed sensor, a commercial respiratory belt sensor (Xinyu Intelligence Co., Ltd) and our RFID humidity sensor have been simultaneously employed to monitor the respiratory signals of the volunteers (Fig. 7h). The volunteers were instructed to follow specific breathing protocols, including different breathing rates as well as simulated abnormal respiratory patterns, namely obstructive sleep apnea (OSA) and central sleep apnea (CSA). The OSA pattern was simulated by holding breath for 10 s followed by two rapid deep breaths, while the CSA pattern was simulated by holding breath for 10 s followed by three normal breaths at a steady rhythm. As shown in Figs. 7i and Fig. S6a, the ΔRSSI waveform of our sensor maintains synchronous alignment with the piezoelectric signal output from the commercial respiratory belt. Both the rising edges of the ΔRSSI signal and the output peaks of the reference sensor correspond to the inhalation phase of the volunteer. Importantly, when the volunteers change their body orientation within certain angular ranges (Fig. S6b), the respiratory signals remain continuous and stable (Fig. S6c). However, the sensor could not capture the respiratory rhythm when it is deliberately covered by the arm (Fig. S6d). Nevertheless, this limitation could potentially be addressed in future work by employing strategies such as multi tag arrangements to enhance signal robustness against physical obstructions. It is worth noting that when compared to LC resonance-based wireless humidity sensors for breath measurement [18,19], our sensor achieves a significantly longer wireless communication distance of up to several tens of centimeters. These distinct advantages collectively establish it as a superior solution for respiratory monitoring applications.

3.10. Comparison of wireless humidity sensors

Table 1 compares the performance of our UHF RFID-based wireless humidity sensor with state-of-the-art flexible wireless humidity sensors. Among those, one category is the active wireless humidity sensing

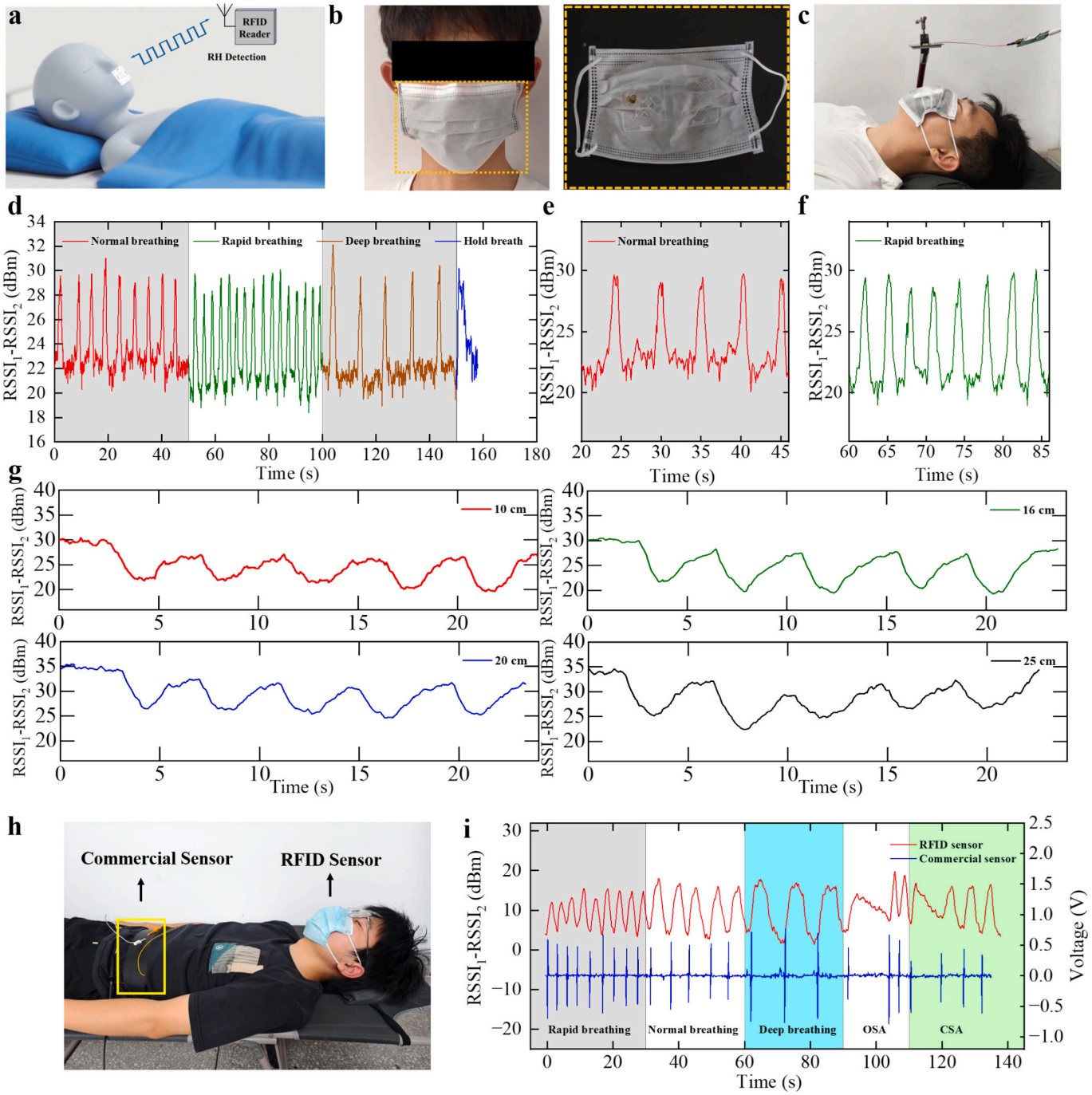

Fig. 7. Respiratory monitoring system built by the UHF RFID humidity sensing system. (a) Conceptual diagram of the UHF RFID wireless humidity sensor for respiratory monitoring during sleep. (b) Photograph of a volunteer wearing a mask with the dural tag-based sensor attached into it. (c) Photograph of the volunteer lying on a bed to mimic the sleep state. The sensor was embedded in the mask and the reader was placed on top of it with a distance of about 10 cm. (d) The time-resolved $RSSI_1$ - $RSSI_2$ signals from the respiratory monitoring system under different breathing modes. A zoomed-in view of the $RSSI_1$ - $RSSI_2$ signals during (e) normal breathing and (f) rapid breathing. (g) The $RSSI_1$-$RSSI_2$ signals during normal breathing with different separation distance between the sensor and the reader. (h) Photograph of simultaneous respiratory monitoring using the UHF RFID sensor and a commercial respiratory belt sensor. (i) Signal comparison between the UHF RFID sensor and the commercial respiratory belt sensor under different breathing states and simulated abnormal breathing patterns.

approach, where the sensor is integrated into an active circuit that converts its output into voltage variations and transmits the data via Bluetooth [35,36]. This design enables a long wireless communication distance. However, the sensor must be coupled with circuitry, resulting in a larger size and loss of device flexibility.

The other category is the passive wireless humidity sensing approach, which primarily relies on monitoring the resonant frequency (f) shift of an LC resonator [17–20,37]. In this method, the device sensitivity is confined by the relationship $f = 1/(2\pi \times \sqrt{LC})$, assuming that the humidity-sensitive parameter is either inductance (L) or capacitance (C). In contrast, the operating mechanism of our UHF RFID-based wireless humidity sensor is fundamentally different. According to Eq. (2), humidity-induced increases in resistance directly modulate the tag gain Gr, which prevents significant sensitivity loss across the entire sensing range. Consequently, our sensor demonstrates the highest sensitivity among comparable devices.

Table 1
Comparison on the Performance of Wireless Humidity Sensors.

Sensing Material	Hysteresis (% RH)	Range (% RH)	Response/Recovery Time (s)	Detection Distance (cm)	Maximum Linear Sensitivity (/%RH)	Wireless Mode	Ref
PI NW /CQD	–	7–97	80/20	–	8.8×10^{-2}	Bluetooth	[35]
rGO /MoS_2	3.43	30–90	0.65/14.4	–	2.6×10^{-3}	Bluetooth	[36]
PI Film	–	24–90	23.4/60.1	3×10^{-3}	2.8×10^{-3}	Inductive Coupling	[17]
MW CNTS /WS_2	–	15–95	7.8/19.6	3	9.83×10^{-4}	Inductive Coupling	[19]
GO/CNT-OH/ Nafion	3	30–95	110/115	–	3.6×10^{-3}	Inductive Coupling	[18]
GO /Mxene	–	20–95	6/37	–	4.9×10^{-3}	Inductive Coupling	[37]
MoS_2	28	40–95	–	1	3.6×10^{-4}	Inductive Coupling	[20]
GO /Mxene	2.9	19–96	8.2/11.4	>30	2.05×10^{-2}	Backscatter	This Work

Additionally, operating in the UHF band allows our sensor to achieve an extended wireless reading distance of several tens of centimeters. This capability, which is unattainable by the existing counterparts, presents a significant benefit for real-world wearable use. There is no similar literature report on this unique feature to our best knowledge.

4. Conclusion

This paper presents a flexible wireless humidity sensor based on UHF RFID technology. Wireless humidity sensing is realized through the incorporation of a humidity-sensitive MGO layer for modulating the tag antenna impedance. Importantly, this paper proposes a humidity sensing strategy with a dual-tag sensor structure. The dual-tag topology effectively mitigates the influence of communication distance variations on measurement accuracy and enhances sensor reliability. The sensor features a simple structure and excellent mechanical flexibility, and successfully recognizes different patterns of respiratory in a real time, offering broad application prospects in the next-generation wearable electronics.

CRediT authorship contribution statement

Jiaqi Zhang: Writing – original draft, Validation, Investigation, Data curation. **Chenbin Zhao:** Visualization, Investigation, Data curation. **Haidong He:** Data curation, Validation. **Donglin Wu:** Investigation, Data curation. **Enting Gao:** Investigation, Funding acquisition. **Changrong Liu:** Supervision, Software. **Xuemei Lu:** Funding acquisition, Formal analysis. **Tao Peng:** Software, Investigation. **Baoqing Nie:** Writing – review & editing, Supervision, Funding acquisition, Conceptualization.

Declaration of competing interest

The authors declare that they have no known competing financial interests or personal relationships that could have appeared to influence the work reported in this paper.

Acknowledgements

This work was supported by the National Natural Science Foundation of China (No. 62471326, No. 22203059), Jiangsu Key Laboratory of Biophotonics Open Projects Fund (Project No. 2025BPT003, No. 2025BPT004), Qing Lan Project.

Appendix A. Supplementary data

Supplementary data to this article can be found online at https://doi.org/10.1016/j.cej.2026.182605.

Data availability

Data will be made available on request.

References

[1] Z.W. Wang, Q.J. Lin, F.Z. Zhang, D. Xian, Q.Z. Meng, M. Zhao, C.H. Li, R. Maeda, Z. D. Jiang, Repurposing traditional China Xuan paper for versatile humidity sensing, Microsyst Nanoeng 12 (2026) 36. ARTN 36, https://doi.org/10.1038/s41378-025-01108-w.
[2] W.H. Dong, X.Y. Chen, Research progress of wearable electrochemical biosensors based on metal-organic frameworks (MOFs) for sweat detection, Adv. Compos. Hybrid Mater. 8 (2025) 310, https://doi.org/10.1007/s42114-025-01357-3.
[3] M.S. Su, W.H. Dong, A.X. Liang, X.Y. Chen, Highly stable and selective flexible sweat sensor combined with bioinspired microfluidic chip: Zn-Ni bimetallic MOF-driven noninvasive renal function assessment, Talanta 305 (2026) 129652, https://doi.org/10.1016/j.talanta.2026.129652.
[4] H. Ma, F. Si, C. He, X. Wang, J. Ding, W. Zhang, X. Fan, Fully printed all-resistive dual-mode sensor with ultra-low temperature coefficient of resistance for crosstalk-free detections of pressure and humidity, Chem. Eng. J. 505 (2025), https://doi.org/10.1016/j.cej.2025.159394, 159394 159394.
[5] H.R. Ma, H.W. Miao, J.J. Shi, J.Q. Wang, Wearable AMC-Based Multimodal Antenna Sensor With GA-BP Network for Plantar Health Monitoring, IEEE Sensors J. 26 (2026) 11084–11096, https://doi.org/10.1109/Jsen.2026.3664812.
[6] J.X. Zou, X.Y. Chen, B. Song, Y.M. Cui, Bionic Spider Web Flexible Strain Sensor Based on CF-L and Machine Learning, ACS Appl. Mater. Interfaces 16 (2024) 23761–23770, https://doi.org/10.1021/acsami.4c02623.
[7] W.H. Dong, X.Y. Chen, J.L. Zhai, X.D. Fang, C.Y. Zhang, Z. Wang, Y.X. Fu, Structure and application of metal-organic frameworks in wearable electrochemical sweat sensors, Trac-Trends in Analytical Chemistry 197 (2026) 118738, https://doi.org/10.1016/j.trac.2026.118738.
[8] A.X. Liang, W.H. Dong, X.Y. Li, X.Y. Chen, A novel dual-mode paper fiber sensor based on laser-induced graphene and porous salt-ion for monitoring humidity and pressure of human, Chem. Eng. J. 502 (2024) 158184, https://doi.org/10.1016/j.cej.2024.158184.
[9] Y. Ni, X. Zang, Y. Yang, Z. Gong, H. Li, J. Chen, C. Wu, J. Huang, Y. Lai, Environmental Stability Stretchable Organic Hydrogel Humidity Sensor for Respiratory Monitoring with Ultrahigh Sensitivity, Adv. Funct. Mater. 34 (2024) 2402853, https://doi.org/10.1002/adfm.202402853.
[10] J. Song, M. Fan, R. Zhang, M. Qu, P. Tang, H. Wang, Y. Bin, Highly sensitive humidity sensor based on composite film of partially reduced graphene oxide and bacterial cellulose, Biosens. Bioelectron. 257 (2024), https://doi.org/10.1016/j.bios.2024.116296, 116296 116296.
[11] A.X. Liang, X.Y. Chen, A non-contact porous composite fiber paper-based humidity sensor for wearable breathing and skin humidity monitoring, J. Mater. Chem. A 12 (2024) 29081–29091, https://doi.org/10.1039/d4ta05393a.
[12] Y. Sun, X. Gao, S. A, H. Fang, M. Lu, D. Yao, C. Lu, Hydrophobic Multifunctional Flexible Sensors with a Rapid Humidity Response for Long-Term Respiratory Monitoring, ACS Sustain. Chem. Eng. 11 (2023) 2375–2386, https://doi.org/10.1021/acssuschemeng.2c06162.
[13] A.X. Liang, J.L. Zhai, J.X. Zou, X.Y. Chen, Porous Carbon Nanoparticle Composite Paper Fiber with Laser-Induced Graphene Surface Microstructure for Pressure

Sensing, Langmuir 41 (2025) 2688–2698, https://doi.org/10.1021/acs.langmuir.4c04486.
[14] Z. Zheng, Y. Zhong, Y. Li, M. Nisar, A. Mansoor, F. Li, S. Chen, G. Liang, P. Fan, D. Xu, M. Wei, Y. Chen, Ultrahigh thermoelectric properties of p-type BixSb2-xTe3 thin films with exceptional flexibility for wearable energy harvesting, Carbon Energy 6 (2024) 541, https://doi.org/10.1002/cey2.541.
[15] N. Sreang, J.-Y. Chung, Miniaturized Antenna Design for Wireless and Powerless Surface Acoustic Wave Temperature Sensors, Sensors 24 (2024) 5490 5490, https://doi.org/10.3390/s24175490.
[16] S. Li, J.R. Hou, Y.P. Xu, L. Guo, R. Zhang, J.H. Pan, Q. Wang, Inkjet-printed wireless passive humidity sensor with ultrahigh sensitivity using ZnO/Ti_3C_2Tx MXene nanocomposite, Meas Sci Technol 37 (2026) 035101. ARTN 035101, https://doi.org/10.1088/1361-6501/ae309d.
[17] Q. Tan, W. Lv, Y. Ji, R. Song, F. Lu, H. Dong, W. Zhang, J. Xiong, A LC wireless passive temperature-pressure-humidity (TPH) sensor integrated on LTCC ceramic for harsh monitoring, Sensors Actuators B Chem. 270 (2018) 433–442, https://doi.org/10.1016/j.snb.2018.04.094.
[18] C. Wang, C. Jiao, M. Wang, J. Pan, Q. Wang, GO/CNT−OH/Nafion Nanocomposite Humidity Sensor Based on the LC Wireless Method, Nanomaterials 13 (2023) 1925, https://doi.org/10.3390/nano13131925.
[19] W. Lv, Q. Tan, H. Kou, W. Zhang, J. Xiong, MWCNTs/WS2 nanocomposite sensor realized by LC wireless method for humidity monitoring, Sensor Actuat. A-Phys. 290 (2019) 207–214, https://doi.org/10.1016/j.sna.2019.03.032.
[20] H. Miao, Y. Gao, X. Biao, F. Xuan, MoS2-Based Flexible LC Sensor With an FCNN Algorithm for Simultaneous Temperature and Humidity Detection, IEEE Sensors J. 23 (2023) 25724–25731, https://doi.org/10.1109/JSEN.2023.3317399.
[21] S. Cho, H. Han, H. Park, S.-U. Lee, J.-H. Kim, S.W. Jeon, M. Wang, R. Avila, Z. Xi, K. Ko, M. Park, J. Lee, M. Choi, J.-S. Lee, W.G. Min, B.-J. Lee, S. Lee, J. Choi, J. Gu, J. Park, M.S. Kim, J. Ahn, O. Gul, C. Han, G. Lee, S. Kim, K. Kim, J. Kim, C.-M. Kang, J. Koo, S.S. Kwak, S. Kim, D.Y. Choi, S. Jeon, H.J. Sung, Y.B. Park, M. Je, Y.T. Cho, Y.S. Oh, I. Park, Wireless, multimodal sensors for continuous measurement of pressure, temperature, and hydration of patients in wheelchair, Npj Flexible, Electronics 7 (2023) 8 8, https://doi.org/10.1038/s41528-023-00238-3.
[22] M. Wagih, Y. Wei, A. Komolafe, R. Torah, S. Beeby, Reliable UHF Long-Range Textile-Integrated RFID Tag Based on a Compact Flexible Antenna Filament, Sensors 20 (2020) 3435 3435, https://doi.org/10.3390/s20123435.
[23] F. Costa, S. Genovesi, M. Borgese, A. Michel, F.A. Dicandia, G. Manara, A Review of RFID Sensors, the New Frontier of Internet of Things, Sensors 21 (2021) 3138 3138, https://doi.org/10.3390/s21093138.
[24] Y. Shao, L. Wei, X. Wu, C. Jiang, Y. Yao, B. Peng, H. Chen, J. Huangfu, Y. Ying, C. J. Zhang, J. Ping, Room-temperature high-precision printing of flexible wireless electronics based on MXene inks, Nature, Communications 13 (2022) 3223 3223, https://doi.org/10.1038/s41467-022-30648-2.
[25] J. Jun, J. Oh, D.H. Shin, S.G. Kim, J.S. Lee, W. Kim, J. Jang, Wireless, Room Temperature Volatile Organic Compound Sensor Based on Polypyrrole Nanoparticle Immobilized Ultrahigh Frequency Radio Frequency Identification Tag, ACS Appl. Mater. Interfaces 8 (2016) 33139–33147, https://doi.org/10.1021/acsami.6b08344.
[26] X. Wang, J. Zhang, Z. Yu, S. Mao, S.C.G. Periaswamy, J. Patton, On Remote Temperature Sensing Using Commercial UHF RFID Tags, IEEE Internet Things J. 6 (2019) 10715–10727, https://doi.org/10.1109/jiot.2019.2941023.
[27] H. An, T. Habib, S. Shah, H. Gao, A. Patel, I. Echols, X. Zhao, M. Radovic, M. J. Green, J.L. Lutkenhaus, Water Sorption in MXene/Polyelectrolyte Multilayers for Ultrafast Humidity Sensing, ACS Appl. Nano Mater. 2 (2019) 948–955, https://doi.org/10.1021/acsanm.8b02265.
[28] A. Ammar, A.M. Al-Enizi, M.A. AlMaadeed, A. Karim, Influence of graphene oxide on mechanical, morphological, barrier, and electrical properties of polymer membranes, Arab. J. Chem. 9 (2016) 274–286, https://doi.org/10.1016/j.arabjc.2015.07.006.
[29] Y. Li, F. Meng, Y. Mei, H. Wang, Y. Guo, Y. Wang, F. Peng, F. Huang, Z. Zhou, Electrospun generation of Ti3C2Tx MXene @graphene oxide hybrid aerogel microspheres for tunable high-performance microwave absorption, Chem. Eng. J. 391 (2020) 123512, https://doi.org/10.1016/j.cej.2019.123512.
[30] B. Li, N. Wu, Y. Yang, F. Pan, C. Wang, G. Wang, L. Xiao, W. Liu, J. Liu, Z. Zeng, Graphene Oxide-Assisted Multiple Cross-Linking of MXene for Large-Area, High-Strength, Oxidation-Resistant, and Multifunctional Films, Adv. Funct. Mater. 33 (2023) 202213357, https://doi.org/10.1002/adfm.202213357.
[31] G. Jia, A. Zheng, X. Wang, L. Zhang, L. Li, C. Li, Y. Zhang, L. Cao, Flexible, biocompatible and highly conductive MXene-graphene oxide film for smart actuator and humidity sensor, Sensors Actuators B Chem. 346 (2021), https://doi.org/10.1016/j.snb.2021.130507, 130507 130507.
[32] E. Mendiburu-Valor, G. Mondragon, N. González, G. Kortaberria, L. Martin, A. Eceiza, C. Peña-Rodriguez, Valorization of urban and marine PET waste by optimized chemical recycling, Resources, Conservation and Recycling 184 (2022), https://doi.org/10.1016/j.resconrec.2022.106413.
[33] F. Gbamele, A. Edouard, C.D. Assamoi, G. Jean, B.T.J. Youan, O. Berenger, K. Fransisco, Study of Mutual Coupling of Typical Commercial UHF RFID Tags in a High-Density Environment, Am. J. Eng. Appl. Sci. 15 (2022) 209–219, https://doi.org/10.3844/ajeassp.2022.209.219.
[34] W.A. Tai, W.T. Hsueh, T.L. Chen, L.M. Fu, Smart masks with breathing sensors: Opportunities and challenges in digital health diagnostics, Sens. Actuators B Chem. 458 (2026) 139846. ARTN 139846, https://doi.org/10.1016/j.snb.2026.139846.
[35] Y. Zhao, H. Yang, Q. Zhang, C. Lei, N. Zhou, R. Shi, L. Shi, J. Wu, H. Luo, H. Mao, A wearable flexible humidity sensor with high-density and large-thickness interdigital electrodes and sensitive CQD bundles for urination monitoring in diapers, Sci. China-Mater. 68 (2025) 1154–1161, https://doi.org/10.1007/s40843-024-3226-6.
[36] N. Ke, F. Si, H. Ma, Q. Gao, G. Ge, W. Liu, J. Ding, W. Zhang, X. Fan, Fully Flexible Humidity Sensor with Fast Response and High Responsivity Based on rGO/MoS2 for Human Respiration Monitoring and Nontouch Switches, ACS Appl. Mater. Interfaces 17 (2025) 2317–2326, https://doi.org/10.1021/acsami.4c18757.
[37] X. Zhang, H. Kou, Z. Shang, L. Yang, Y. Wang, Research on flexible LC wireless humidity sensor based on GO/Mxene, Journal of Electronic Measurement and Instrumentation 38 (2024) 154–160.